



CHORUS

This is the accepted manuscript made available via CHORUS. The article has been published as:

Effects of pulse shape on strongly driven two-level systems

C. W. S. Conover

Phys. Rev. A **84**, 063416 — Published 19 December 2011

DOI: [10.1103/PhysRevA.84.063416](https://doi.org/10.1103/PhysRevA.84.063416)

Effects of Pulse Shape on Strongly Driven Two-Level Systems

C. W. S. Conover*

Department of Physics and Astronomy, Colby College, Waterville, ME 04901

(Dated: November 11, 2011)

We present an experimental study of the dynamics of a two-level system driven by strong non-resonant electromagnetic pulses as a function of pulse intensity and detuning. We have explored the qualitative and quantitative behavior of the transition probability as a function of pulse area for five different temporal profiles: Lorentzian, Lorentzian squared, hyperbolic secant, hyperbolic secant squared, and Gaussian. The two-level system consists of a fine-structure doublet in sodium Rydberg states coupled by Raman transitions driven through far-off-resonance intermediate states. The pulses are in the microwave regime and have high fidelity and uniform intensity. Experiments show that despite the similarity in the pulse shapes, the behavior of the population transfer versus intensity depends dramatically on the temporal shape and that the spectral properties and area of the pulse do not adequately describe the response.

PACS numbers: 32.80.Rm 32.30.Bv 32.60.+i 42.50.Hz

I. INTRODUCTION

A fundamental quantum dynamical process is the evolution of a two-level quantum system driven by a strong, time-dependent, coherent radiation field. This deceptively simple system has been the subject of intense and longstanding theoretical and experimental investigation [1–3]. The goal of this paper is to experimentally demonstrate the dramatic effect that relatively small changes in pulse shape of non-resonant radiation can have on the intensity dependence of the transition probability in two-level systems. We explore this problem with “bell-shaped” pulse shapes typified by the hyperbolic secant which is the only smooth, symmetric coupling pulse shape for which an analytic solution to two-level dynamics has been found [4].

In addition to fundamental interest, the nonperturbative dynamics of two-level systems has a practical application in quantum information science, where precise control of coherent evolution is required. The need to control the evolution of two-level systems driven by near-resonant pulses arises in the manipulation of quantum bits in universal quantum processors. Examples occur in implementing operations on Josephson-junction, quantum-dot, or trapped ion qubits where the desire to use short intense pulses for fast operations can be in conflict with the desire to not excite additional nearby states [5–10]. Judicious choice of pulse shapes could significantly reduce errors due to off-resonant coupling to additional states.

The behavior of two-level systems can also provide insight into quantum dynamics of more complex systems. For example, an important general question in the field of coherent control is whether it is possible to use intensity to compensate for detuning in transferring population between quantum states and how to understand the nonperturbative regime where the spectral properties of the pulse no longer fully define a system’s response [11–14]. Knowledge of the general behavior of transition probability for different pulse shapes as a func-

tion of intensity may be important to affecting control, particularly when the goal is to determine the appropriate pulse shape to minimize or maximize a transition probability for a given detuning from resonance.

Despite its simplicity, and even after invoking the rotating wave approximation, there are a remarkably limited number of situations for which the dynamics of a two-level system can be solved in closed form. The Schrödinger equation for such a system is written in the field-interaction representation in terms of the probability amplitudes b_i and b_f as:

$$i \begin{pmatrix} \dot{b}_i \\ \dot{b}_f \end{pmatrix} = \frac{1}{2} \begin{pmatrix} -\Delta(t) & \Omega^*(t) \\ \Omega(t) & \Delta(t) \end{pmatrix} \begin{pmatrix} b_i \\ b_f \end{pmatrix} \quad (1)$$

where the coupling between the two states is defined by the Rabi frequency, $\Omega(t) = \Omega_o G(t)$ and the detuning from resonance is given by $\Delta(t)$. $G(t)$ is the temporal profile, with a width scale τ , of the driving field. In this Hamiltonian spontaneous emission is ignored during the time evolution of the wavefunction.

In general, solutions to Eq. 1 with constant detuning, $\Delta(t) = \Delta_o$, show two characteristics: oscillation of the populations with intensity (Rabi oscillations) and a decrease in the oscillation amplitude with detuning from resonance [1–3].

If the driving field is resonant, $\Delta(t) = 0$, then the population transfer is independent of pulse shape, depending only on the area

$$S = \Omega_o \int_{-\infty}^{\infty} G(t) dt \equiv \Omega_o \tau, \quad (2)$$

of the pulse, where the integral of the temporal profile is τ . A system initially in state $|i\rangle$ has a probability amplitude

$$b_f(t \rightarrow \infty) = -i \sin\left(\frac{S}{2}\right) \quad (3)$$

after any pulse of area S , with periodic maxima and returns to zero. Robinson [15] showed that temporally symmetric non-resonant pulses always have finite values of the area, called return areas and denoted S_n , for which the population transfer will vanish.

* cconover@colby.edu

In the perturbative limit, $S \ll \pi$, the transition amplitude, b_f , is given by

$$\begin{aligned} b_f(t \rightarrow \infty) &= -i \frac{(\Omega_o \tau)}{2} \left\{ \frac{1}{\tau} \int_{-\infty}^{\infty} G(t) e^{+i\Delta_o t} dt \right\} \\ &= -i \frac{S \sqrt{2\pi}}{2} \tilde{G}(\Delta_o). \end{aligned} \quad (4)$$

where $\tilde{G}(\Delta_o)$ is the Fourier transform of the temporal profile evaluated at the detuning. When $\Delta_o \tau \gg 1$ the pulse does not contain Fourier components that compensate for the detuning, and the probability of transfer to state f is small. This calculation is the basis for the energy-time uncertainty principle.

For strong nonresonant pulses with constant detuning analytical solutions to Eq. 1 are known only for a few specialized cases. The Rosen-Zener solution [4] for the hyperbolic-secant pulse $G(t) = \text{sech}(\pi t/\tau)$ is

$$b_f(t \rightarrow \infty) = -i \sin\left(\frac{S}{2}\right) \text{sech}\left(\frac{\Delta_o \tau}{2}\right), \quad (5)$$

depending only on the area of the pulse and $\Delta_o \tau$, which we refer to as the scaled detuning. Of particular note is the fact that the amplitude of the Rabi oscillations are dependent only on the scaled detuning and not on the Rabi frequency, and that the return areas are the same as for a resonant pulse, $S_n = 2n\pi$. Rosen and Zener recognized that $\text{sech}(\frac{\Delta_o \tau}{2})$ is $\frac{\sqrt{2\pi}}{\tau} \tilde{G}(\Delta_o)$ for the hyperbolic secant pulse, and that the solution is consistent with the uncertainty principle argument derived from perturbation theory. Further, they conjectured that an arbitrary envelope function would produce a transition probability

$$P_f = \sin^2\left(\frac{S}{2}\right) \left| \frac{\sqrt{2\pi}}{\tau} \tilde{G}(\Delta_o) \right|^2. \quad (6)$$

Their conjecture is known to be invalid in general. For example, the well-known Rabi solution for a square pulse with width τ

$$P_f = \frac{\Omega_o^2}{\Omega_o^2 + \Delta_o^2} \sin^2\left(\frac{1}{2} \sqrt{\Omega_o^2 + \Delta_o^2} \tau\right), \quad (7)$$

does not obey the Rosen-Zener conjecture. In Eq. 7 the amplitude of the Rabi oscillations tends toward unity for large Rabi rates, no matter what the detuning, and the return areas occur for

$$S_{n,\text{Rabi}} = \Omega_o \tau = 2n\pi \sqrt{1 - \frac{1}{n^2} \left(\frac{\Delta_o \tau}{2\pi}\right)^2} \leq 2n\pi. \quad (8)$$

However, the square pulse is clearly not experimentally realizable and the spectrum has mathematical artifacts from the temporal discontinuities.

Failure of the Rosen-Zener conjecture was also shown explicitly by Bambini and Berman for a class of asymmetric pulses that can be mapped onto the Rosen-Zener solution [16]. With asymmetric pulses, the oscillatory solutions do not return to zero for any finite pulse intensity. However, the Eq. 6

has been shown to hold approximately in a wide variety of situations [15, 17–19], when the pulses are not too strong, the scaled detuning $\Delta_o \tau$ is small, and the pulses have smooth spectra.

A reasonable question, then, is whether there are general trends for the magnitude of the Rabi oscillations and the return areas as a function of pulse intensity and detuning. The major goal of this paper is to experimentally explore the quantitative and qualitative features of the population transfer due to different symmetric pulse shapes as a function of pulse intensity and detuning from resonance.

More than a decade ago Berman and coworkers [20] showed that with detunings that are large compared to the pulse bandwidth, the qualitative behavior of the solutions for different pulse shapes can be dramatically different. In particular they showed that for far-detuned pulses with large pulse areas that Lorentzian and Lorentzian-squared pulses produce Rabi oscillations with amplitudes decreasing in magnitude with pulse area, while Rabi oscillations with hyperbolic secant and hyperbolic secant squared pulses produce constant amplitude Rabi oscillations and Gaussian pulses produce Rabi oscillation amplitudes that increase with pulse area. Robinson [15, 21–24] showed that the return areas are systematically different from $S_n = 2n\pi$ for different pulse shapes. In particular, he predicted $S_n > 2n\pi$ for Lorentzian shaped pulses and $S_n < 2n\pi$ for Gaussian and other smooth pulse shapes. Prior experiments that have looked at Rabi oscillations as a function of intensity [10, 25–31] have been insensitive to these pulse-shape dependencies either because of the inability to precisely control or measure the pulse shape, fluctuations in the pulse intensity, or because of the short lifetime in the excited state.

We demonstrate the trends predicted by Berman *et al.* [20] and Robinson [15, 21–24] using an effective two-level system. We will show that the behavior elucidated by Berman *et al.* [20] is not limited to the large detuning regime, but can be important even when the detuning is small. Further, the general behavior of the solutions is not affected by the precise Hamiltonian and the inclusion of time-dependent detunings through AC Stark shifts does not affect the overall qualitative behavior. Like Berman *et al.* [20] we find that the behavior of the two-level transition probability can be understood in terms of the ratio of the instantaneous energy difference between the eigenstates of Eq. 1 and the rate at which the eigenstates of Eq. 1 themselves change as the pulse turns on and off.

II. EXPERIMENTAL APPROACH AND APPARATUS

A. Overview

Experimental exploration of the physics defined by Eq. 1 requires a two-level system where the excited state has a long radiative lifetime and the interaction with the electromagnetic field can be precisely controlled. We chose to make measurements of Raman transitions between fine-structure doublets in Rydberg states. The Hamiltonian for the system is given by Eq. 1 when all of the intermediate states are adiabatically eliminated as outlined in Appendix A.

Rydberg states are nearly ideal for the experiments. First, the states are closely spaced, making possible experiments with microwave fields, where high-fidelity pulses with precisely measured uniform amplitudes are readily produced. Second, they have large dipole moments which allows strong Raman coupling with modest fields. Despite small ($\simeq 10$ MHz) spacing between the two states they can be efficiently and selectively detected by ionizing the atoms with a ramped electric field. Third, Rydberg states have radiative lifetimes that are long compared to the pulse widths we employ. Finally, Rydberg systems can be accurately modeled with relatively simple numerical techniques for comparison with the experimental results.

In the experiments we measured $\Delta m_j = 0$ transitions between $|i\rangle = |23d_{3/2} |m_j| = \frac{1}{2}\rangle$ and $|f\rangle = |23d_{5/2} |m_j| = \frac{1}{2}\rangle$ driven by z-polarized 650 MHz pulses. The quantum defect of the nd states in sodium is $\delta_2 = 0.015$ [32], and the $23d$ doublet is isolated from any other state by least 7.5 GHz. Raman coupling is through far-detuned np and nf states. Because of their spacing from other states, the $23d$ states have only small Stark mixing with other angular momentum states for static electric fields less than 15 V/cm. While we present results only for $23d$ states, similar behavior was seen for different principal quantum numbers.

B. Model Parameters

As outlined in Appendix A for Rydberg doublets the two-level Hamiltonian of Eq. 1 is defined by three parameters, the zero-field detuning Δ_o , the peak Rabi frequency Ω_o , and the peak differential AC Stark shift Δ_d . These parameters determine the time-dependent two-photon Rabi frequency $\Omega(t) = \Omega_o G(t)$, and the time-dependent detuning $\Delta(t) = \Delta_o + \Delta_d G(t)$, where $G(t)$ is the intensity profile of the pulse.

We have measured $\Delta_o/2\pi = -7.95 \pm 0.01$ MHz using time-domain spectroscopy [33]. In order to determine Ω_o and Δ_d , defined in Eq. A10 and Eqs. A14 and A9, we computed the dipole matrix elements $d_{pq} = -e\langle p|z|q\rangle$ using a Numerov algorithm [34] and the known quantum defects of the sodium Rydberg states [32]. We calculated Ω_o and Δ_d using the nearest three pairs of f states and the nearest four pairs of p states in the set of intermediate levels. Adding more intermediate states does not change the calculated parameters at more than the 0.1% level, as the matrix elements get smaller and the energy denominators get larger for more distant states. We determine that for 650 MHz pulses

$$\begin{aligned} \frac{\Omega_o}{2\pi} &= 2.25 \frac{\text{MHz}}{(\text{V/cm})^2} \mathcal{E}_o^2 \\ \frac{\Delta_d}{2\pi} &= 0.432 \frac{\text{MHz}}{(\text{V/cm})^2} \mathcal{E}_o^2. \end{aligned} \quad (9)$$

To assess the accuracy of these parameters we measured the electric-field dependent change in the spacing of the $23d$ $m_j = 1/2$ fine structure states. The field-dependent split-

ting is

$$\Delta(\mathcal{E}) = \Delta_0 + \alpha_{n\ell}^T \left\{ \frac{12m_j^2}{(2\ell-1)(2\ell)(2\ell+1)} \right\} \mathcal{E}^2, \quad (10)$$

where \mathcal{E} is the static electric field and $\alpha_{n\ell}^T$ is the tensor polarizability [35]. We measured $\alpha_{23d}^T/2\pi = 18.8 \pm 0.1$ MHz/(V/cm)². Calculation of the tensor polarizability, which depends on the same matrix elements and energy differences as Ω_o and Δ_d [35–38], gives $\alpha_{23d}^T/2\pi = 18.3$ MHz/(V/cm)², a difference of less than 3% from the measured value. We assume that the accuracy of the parameters in Eq. 9 is similar.

C. Rydberg Atom Production and Detection

Experiments are performed in a vacuum chamber with a background pressure of 5×10^{-7} Torr. An atomic beam of sodium is emitted from a resistively heated oven and passes through a transmission line perpendicular to the propagation of the microwave pulse as diagrammed in Fig. 1a. The atoms are excited in a stepwise manner, from the $3s_{1/2}$ to the $3p_{1/2}$ state and then to the $23d_{3/2}$ Rydberg state by 589 nm and 410 nm nanosecond dye lasers pumped, respectively, by the second and third harmonics of a 20 Hz Nd:YAG laser. The laser beams are nearly collinear and propagate antiparallel to the atomic beam. The lasers are polarized to excite only the $m_j = \pm \frac{1}{2}$ states.

About 100 ns after the Rydberg state is populated the microwave pulse is applied to the transmission line. Following the microwave pulse a slow (microsecond timescale) high voltage ramp is applied to a capacitively isolated plate of the transmission line. During the ramp the angular momentum states adiabatically evolve into Stark states which ionize at distinct electric fields [39]. Following ionization the electric field pushes the free electrons into a microchannel-plate detector, with the electrons from atoms in the $d_{5/2}$ state arriving before those from atoms in the $d_{3/2}$ state as shown in Fig. 1b. Using both signals it is possible to determine an absolute transition probability.

Absolute probabilities were determined by integrating the area of the $d_{5/2}$ peak after subtracting the small background without the yellow 3s-3p laser, and normalizing to the total electron signal. A small ambiguity in the final state distribution arises because electrons from the two states are not completely distinguishable, as seen by the overlap of the wings of the two peaks in Fig. 1b. We attribute the overlap to some nonadiabatic evolution during the field-ionization pulse. The presented results are adjusted with the assumption that a constant fraction of electrons detected in the $d_{5/2}$ peak are from the $d_{3/2}$ state and vice-versa. We determined the correction factor using measurements made with no RF pulse, when only the $23d_{3/2}$ state was excited. We measure approximately 5% of the electrons within the $23d_{5/2}$ peak under these conditions. Assuming that the overlap is independent of the initial state is essentially an assumption that the field ionization process is incoherent. The assumption affects only the overall size of the

measured population transfer, but not the shape of the population transfer curves or the fields where maxima and minima of the population transfer occur, which are the main concerns of this paper.

The experiment is run synchronously with the 60 Hz AC electrical line and the experiments are performed at the zero crossing of line currents in the laboratory to reduce the effect of magnetic fields, which are mainly from the sodium oven, in the apparatus. In addition, the transmission line was located at the center of a long mu-metal box with open ends which shields the interaction region and reduces the residual magnetic field in the transmission line to less than 100 mG. In zero magnetic field the $m_j = \pm \frac{1}{2}$ states behave identically and in our discussion we neglect magnetic field interactions.

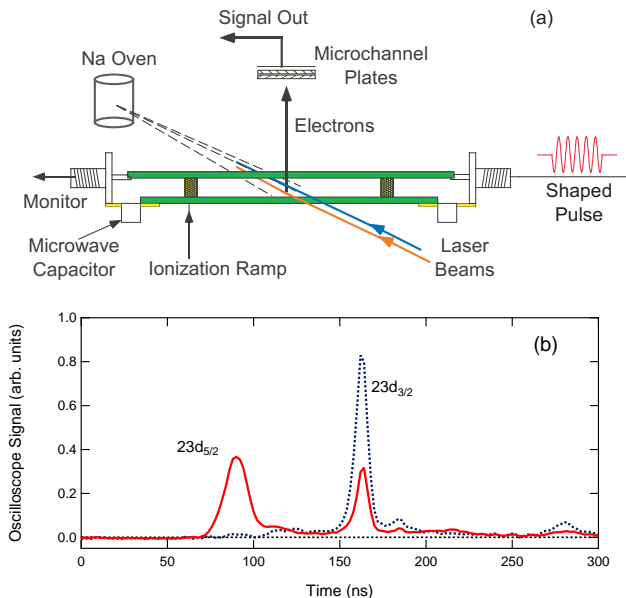


FIG. 1. (Color online) (a) Overview of the experimental apparatus showing the parallel plate transmission line, atomic source, and microchannel plate detectors. (b) Experimental traces showing the signal from the microchannel plate detector without (blue, dashed) a microwave pulse and following application of a 12.5 ns Gaussian pulse with amplitude of approximately 3.75 V/cm (red, solid). The zero of the time-scale is shortly before the peak of the ionization pulse.

D. Microwave pulses

We generate an electromagnetic field having the form

$$\begin{aligned} \mathcal{E}(t) &= \mathcal{E}_o |g(t)| \cos(\omega_o t - \phi(t)) \hat{e} \\ &= \frac{1}{2} \mathcal{E}_o (g(t) e^{-i\omega_o t} + g^*(t) e^{i\omega_o t}) \hat{e} \end{aligned} \quad (11)$$

with peak magnitude \mathcal{E}_o and polarization \hat{e} . In this paper, we consider only functions $g(t)$ with constant $\phi(t)$. The envelope function $g(t)$ determines the Rabi frequency and AC Stark shift profiles, with $G(t) = |g(t)|^2$.

To generate the shaped microwave pulses we modulate the output of a 650 MHz continuous wave oscillator (Rohde &

Schwarz SME03) phase locked to a 10 MHz laboratory clock. The microwaves were modulated in an I&Q modulator (Merrimac Industries IQM-9B-500) using the output of a 1 GS/s arbitrary waveform generator (Tektronix AWG520) which was also phase locked to the 10 MHz clock. This pulse shaper is capable of modulating both the phase and the amplitude of the microwave pulses, but for this experiment only amplitude modulation was used since the Hamiltonian depends only on the intensity of the pulses. In practice we are interested in specific $G(t)$ and program their square roots into the pulse shaper.

A reasonable way to characterize the output pulses is by their fidelity to the programmed pulse shape, defined as the absolute square of the overlap

$$\mathcal{F} = \left| \int g_p^*(t) g_m(t) dt \right|^2, \quad (12)$$

between the programmed and measured pulse shapes, $g_p(t)$ and $g_m(t)$. We measured the fidelity of the pulses using a LeCroy 960 2 GHz bandwidth oscilloscope.

Fidelity of the pulses was improved over a straightforward implementation by (a) adding a small DC offset to each of the IF ports of the I&Q modulator which reduced carrier leakage by 22 dB, enhancing the on/off contrast and (2) filtering the output with a 1 GHz low-pass filter which reduces the harmonic output by more than 20 dB. With the steps taken, the pulses have $\mathcal{F} \geq 0.995$ just before entering the transmission line.

After shaping, the pulses are attenuated by step attenuators and their intensity is scanned using a General Microwave D1961B voltage controlled attenuator. The attenuator has a nominal attenuation of 10 dB per volt, but the variation from the nominal value is significant (± 1 dB), and the attenuation was calibrated using the digital oscilloscope. Pulses were amplified to 1 W using a Minicircuits ZHL 2-12 amplifier which has a maximum linear output of 29 dBm and a gain of 24 dB. Measurements of the pulses after the amplifier show no degradation of fidelity.

The design of the transmission line has been described earlier [40]. The version used in these experiments consists of two parallel brass plates approximately 15 cm long that have a 50 Ω impedance; the plate separation is 0.762 cm and their width is 5.72 cm. The signal to the top plate is coupled from a coaxial cable by a standard SMA connector and passes to a monitor via a second SMA connector and coaxial cable. The lower plate is connected to each SMA ground via a 100 pF microwave capacitor. The capacitors allow the application of the slowly varying ionization ramp while only minimally affecting the transmission of the microwaves. Using a directional coupler, we have determined that the total reflected power from the transmission line is less than 5%. The relatively short length of the transmission line means that except for pulses with durations comparable to the 1 ns round trip time of the low-finesse cavity, that the only effect of reflections is a small change in the amplitude and phase of the pulse within the transmission line. We calibrated the field inside the transmission line using an Avtech Electrosystems AVX-BP1 probe

and the peak field calibration is based on these measurements. We estimate that between the residual nonlinearities in the attenuator and amplifier and the calibration of the peak field that the uncertainty in \mathcal{E}_0 is less than 5%.

III. RESULTS

Experiments were performed with five different pulse shapes, (a) Lorentzian, (b) Lorentzian squared, (c) hyperbolic secant, (d) hyperbolic secant squared, and (e) Gaussian. The temporal intensity profiles

$$G_a(t) = \frac{1}{\left(1 + \left(\frac{\pi t}{\tau}\right)^2\right)} \quad (13a)$$

$$G_b(t) = \frac{1}{\left(1 + \left(\frac{\pi t}{2\tau}\right)^2\right)^2} \quad (13b)$$

$$G_c(t) = \text{Sech}\left(\frac{\pi t}{\tau}\right) \quad (13c)$$

$$G_d(t) = \text{Sech}^2\left(\frac{2t}{\tau}\right) \quad (13d)$$

$$G_e(t) = e^{-\pi\left(\frac{t}{\tau}\right)^2} \quad (13e)$$

are shown graphically in Fig. 2(a). Each pulse is generally bell-shaped, with equal maxima and an area τ so that the pulse area S , defined in Eq. 2, is identical for the same peak intensity.

While all five pulses are quite similar in shape, there are clearly some differences. As can be seen in Fig. 2(a), differences between the Lorentzian squared, hyperbolic secant, and hyperbolic secant squared pulses are very small. On the other hand, the Gaussian and Lorentzian have notable differences from the hyperbolic secant in their temporal structure. The Gaussian falls to zero comparatively rapidly in the wings of the pulse, but quite slowly for $t/\tau \ll 1$. The Lorentzian, on the other hand, falls to zero quite slowly in the wings of the pulse but relatively quickly for $t/\tau \ll 1$. The Lorentzian squared is intermediate between the Lorentzian and hyperbolic secant shapes, while the hyperbolic secant squared pulse is intermediate between the hyperbolic secant and the Gaussian shapes.

In the frequency domain, the five different pulse shapes

$$\tilde{G}_a(\Delta) = \frac{\tau}{\sqrt{2\pi}} e^{-|\Delta|\tau/\pi} \quad (14a)$$

$$\tilde{G}_b(\Delta) = \frac{\tau}{\sqrt{2\pi}} \left(1 + \frac{2|\Delta|\tau}{\pi}\right) e^{-\frac{2|\Delta|\tau}{\pi}} \quad (14b)$$

$$\tilde{G}_c(\Delta) = \frac{\tau}{\sqrt{2\pi}} \text{Sech}\left(\frac{\Delta\tau}{2}\right) \quad (14c)$$

$$\tilde{G}_d(\Delta) = \frac{\tau}{\sqrt{2\pi}} \left(\frac{\pi\Delta\tau}{4}\right) \text{Csch}\left(\frac{\pi\Delta\tau}{4}\right) \text{Sech}\left(\frac{\pi\Delta\tau}{4}\right) \quad (14d)$$

$$\tilde{G}_e(\Delta) = \frac{\tau}{\sqrt{2\pi}} e^{-\frac{(\Delta\tau)^2}{4\pi}} \quad (14e)$$

are shown graphically in Fig. 2(b) versus the scaled detuning $\Delta\tau/2\pi$. All decrease exponentially at large detuning. Behav-

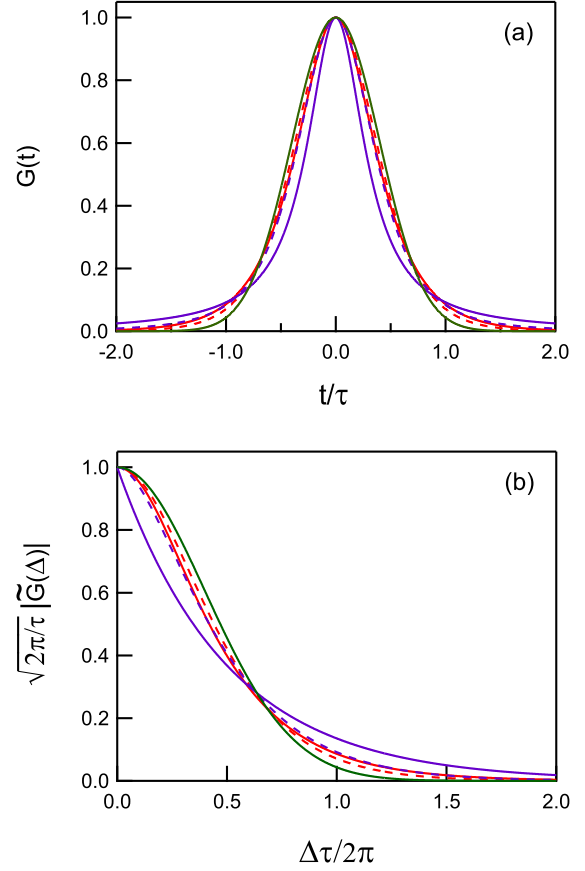


FIG. 2. (Color online) Plots of the five pulse shapes in the (a) time- and (b) frequency-domain. The shapes are Lorentzian (solid, lavender), Lorentzian squared (dashed, lavender), hyperbolic secant (solid, red), hyperbolic secant squared (dashed, red), and Gaussian (solid, green).

iors in the time-domain are reflected in the frequency domain, with the Gaussian having significantly less and the Lorentzian significantly more spectral energy than a hyperbolic secant pulse at large scaled detunings. Again, for small scaled detunings the characteristics of the Gaussian and Lorentzian are reversed. A further important distinction is that while all five pulse shapes are smooth in the time domain, the Lorentzian has a discontinuous derivative at $\Delta\tau = 0$.

Because the detuning is fixed at 7.95 MHz by the atomic structure, we adjust the scaled detuning $\Delta_o\tau$ by changing the length of the pulse, and therefore its spectral bandwidth. This means that pulses of the same peak intensity but different detunings also have different areas. We performed experiments with pulse widths τ ranging from 12.5 ns to 75 ns. The corresponding scaled detunings $\Delta_o\tau/2\pi$ range from 0.1 to 0.6. In the frequency domain the corresponding intensity spectra have bandwidths ranging roughly from 35 MHz to 6 MHz.

Results of population transfer as a function of intensity for each pulse shape are shown in Figs. 3-7. The peak field strengths \mathcal{E}_0 were scanned from zero to approximately 7 V/cm with data points separated approximately evenly in \mathcal{E}_0^2 . The

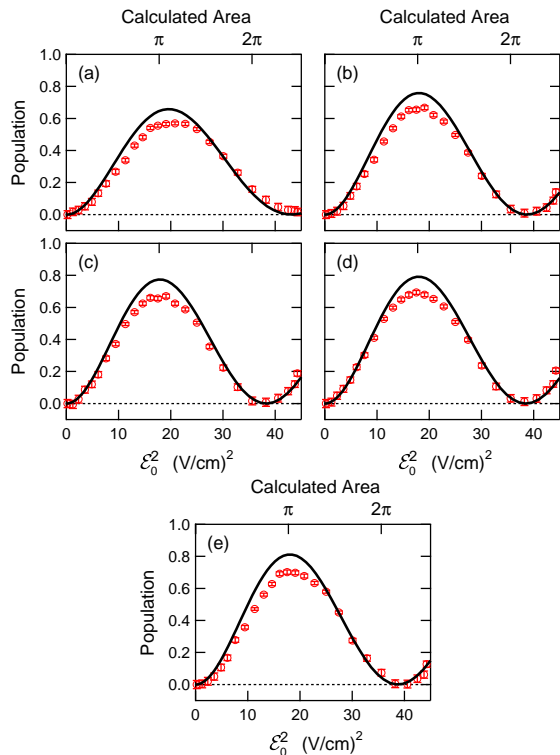


FIG. 3. (Color online) This graph shows the population transfer for (a) Lorentzian, (b) Lorentzian squared, (c) hyperbolic secant, (d) hyperbolic secant squared, and (e) Gaussian 12.5 ns pulses as a function of the square of the pulses' peak electric field. These pulses have a scaled detuning $\Delta_o\tau/2\pi = 0.1$. The solid lines are the result of a multi-level calculation described in Appendix B. These lines are scaled in \mathcal{E}_o^2 by a factor of 1.075, but no scaling of the population transfer was applied. The pulse areas along the top axis are calculated from Eq. 2 using the two-level approximation of the Rabi frequency from Eq. A10.

corresponding two-photon Rabi rates $\Omega_o/2\pi$ and relative AC Stark shifts $\Delta_d/2\pi$ ranged up to approximately 100 MHz and 20 MHz respectively, both significantly larger than the zero-field detuning. At these field strengths no transitions to states other than the $23d_{5/2}$ state were observed although at significantly larger fields (over 15 V/cm), transitions to the $23f$ and higher angular momentum states occur [41].

The error bars in each plot represent the statistical uncertainty of the raw data and the uncertainty due to the ambiguity introduced by the imperfect separation of the two electron pulses seen in Fig. 1(b). Each graph is labeled horizontally with both the squared electric field, and the pulse area $S = \Omega_o\tau$ calculated based on the Rabi rate of Eq. 9.

Each plot also contains a solid line which is the result of a calculation of the population transfer based on the model described in Appendix B. The calculation explicitly includes the evolution of the nearest set of intermediate states ($23f$). At high fields, adiabatic elimination of these states leads to inaccurate values of the parameters of Eq. 9. In addition, the model calculation includes additional high- ℓ states that are strongly coupled to the $23f$ states. Finally, the \mathcal{E}_o^2 values

for the computed transition probability have been scaled by a factor of 1.075 to more closely agree with the experimental results. Equivalently, the dipole matrix elements used in the calculation could have been scaled down by $\sqrt{1.075}$, reducing the theoretical Rabi rate by 7.5%. The scaling required is in rough agreement with the discrepancy measured in the tensor polarizability, but is likely due to a combination of error in the matrix elements and the experimental field calibration.

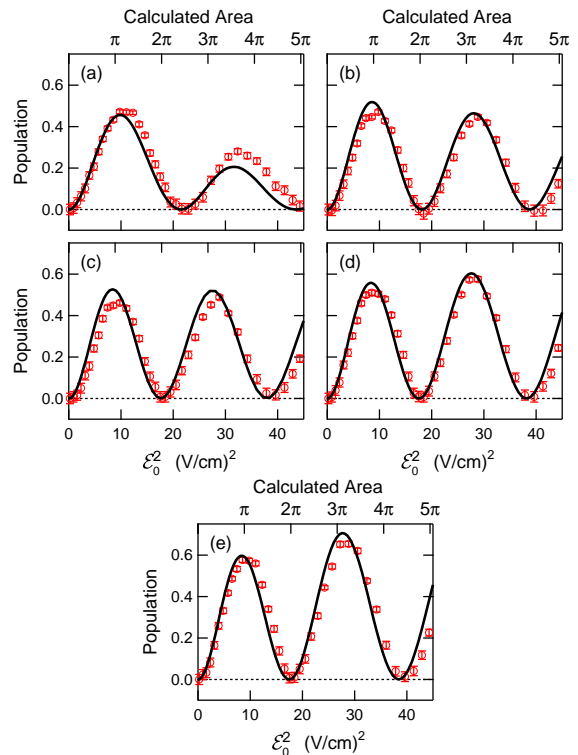


FIG. 4. (Color online) The same as Fig. 3 for 25 ns pulses. These pulses have a scaled detuning $\Delta_o\tau/2\pi = 0.2$.

As expected for symmetric pulses, the population transfer exhibits Rabi oscillations, with peaks and returns to zero population transfer as a function of pulse intensity for all of the pulse shapes. The peak population transfer decreases for longer pulse durations (larger scaled detuning), as would be expected by both uncertainty principle arguments and the Rosen-Zener conjecture.

In general the experimental results agree with the computed transition probability in the amplitude of the Rabi oscillations and, after scaling the theoretical field strengths, the locations of the peaks and zeros of the transition probability. For the shortest experimental pulses presented in Fig. 3, the computed transition probability is systematically larger than the experimental results. We attribute this discrepancy to imperfections in the shape of the pulse, due to (1) their large bandwidth which is approaching the nominal bandwidth of the modulator and (2) small reflections at the end of the transmission line which would slightly stretch its length. These imperfections in the pulses become less important for longer pulses, and indeed agreement between the numerical model and the

experimental results are better for the longer pulses shown in Figs. 4-7.

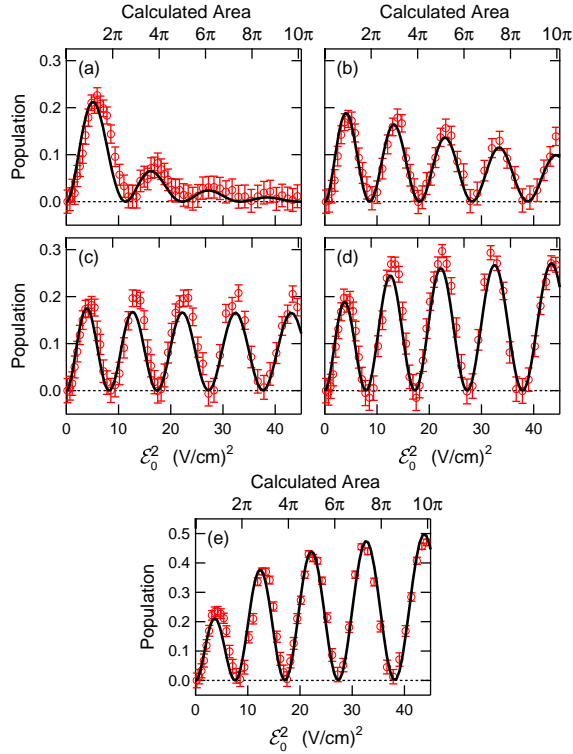


FIG. 5. (Color online) The same as Fig. 3 for 50 ns pulses. These pulses have a scaled detuning $\Delta_o\tau/2\pi = 0.4$. The vertical scale for Gaussian results is twice what it is for the other four pulse shapes.

Focussing for the moment on the first maximum of the Rabi oscillations, where the Rosen-Zener conjecture is most likely to approximately hold, the systematic variations in the response to different pulse shapes might be predicted based on the spectral intensities of Eq. 14. Results for pulses with $\Delta_o\tau/2\pi = 0.1$ ($\tau = 12.5$ ns), seen in Fig. 3 show that for all pulses except the Lorentzian the experimental peak population transfer is approximately 70%, but the Lorentzian maximum is slightly less than 60%. On the other hand, results for the largest scaled detunings with $\Delta_o\tau/2\pi = 0.6$ ($\tau = 75$ ns), as seen in Fig. 7, show that the situation is reversed, with the first Rabi peak of the Lorentzian pulse having approximately twice the population transfer (10%) of the other pulse shapes. A smooth transition between these two readily observable quantitative differences is apparent for the intermediate length pulses with $\Delta_o\tau/2\pi = 0.2, 0.4, \text{ and } 0.5$.

As shown graphically in Fig. 2(b), the Rosen-Zener conjecture for the amplitude of the Rabi oscillations qualitatively agrees with these observations, as the Lorentzian's spectral intensity is significantly lower than the other pulses' at small scaled detuning and significantly higher at large scaled detuning. However, a quantitative determination of the spectral intensities at $\Delta_o\tau/2\pi = 0.1$ and 0.2 shows that the predicted ratios of the Lorentzian and Gaussian peak heights are 1.4 and 1.75, which is far from what is observed. In addition, for

$\Delta_o\tau/2\pi = 0.6$ the spectral intensities are nearly the same, but experimentally the ratio of the Lorentzian to Gaussian peak height is approximately two.

It is tempting to attribute these differences to the added detuning of the AC Stark shifts which are not included in Eq. 6. AC Stark shifts tend to increase the average energy spacing during the pulse, giving each pulse an effective scaled detuning somewhat larger than $\Delta_o\tau$. This would move the ratios of spectral intensities closer to the experimentally observed ratios of the first Rabi peak. However, the maximum AC Stark shift at the fields of the first Rabi peak gives $\Delta_d\tau/2\pi \approx 0.1$, which is insufficient to close the quantitative gap between the experimental peak heights and predictions based on the spectrum.

Of course, the most remarkable property of the data is the clear systematic variation in the Rabi oscillation amplitudes as a function of intensity seen in Figs. 4-7. While the hyperbolic secant pulses produce Rabi oscillations with almost constant amplitude, the Lorentzian and Lorentzian squared pulses produce Rabi oscillation amplitudes that decrease with intensity, while the hyperbolic secant squared and Gaussian pulses produce Rabi oscillation amplitudes that increase with intensity. The Rabi oscillations due to the hyperbolic secant squared pulse seem to level off at large pulse area, but the amplitude of the Rabi oscillations due to a Gaussian pulse continue increasing with area.

The differences between the results of Lorentzian and Gaussian pulses are particularly dramatic, and show that details of the pulse shape significantly affect the strong-field response. The observed behavior is consistent with the findings of Berman *et al.* [20] for large detunings. However, even for pulses where the bandwidth is twice as large as the detuning (Fig. 4) the intensity dependence of the response to different pulse shapes is significantly different.

Further observation of the data shows in addition that the zeros of the Rabi oscillations for the Lorentzian pulses are located at dramatically different pulse intensities than any of the other pulses. For example, in Fig. 3 the zero of the population transfer occurs at 44 (V/cm)², while the other four pulses have zeros at approximately 38 (V/cm)², corresponding to a 15% larger pulse area required for a nominally 2π pulse. Likewise, for all of the other pulse widths, the Lorentzian pulse has zeros of the transition probabilities at intensities that are significantly larger than the other four pulses. This difference is not an artifact of cutting off the Lorentzian pulse experimentally; the pulses were experimentally defined between $\pm 7.5\tau$, which would account for less than a 3% reduction in the pulse area. The locations of the zeros of the transition probabilities of the other pulses are all very close to each other, but show small systematic differences which will be discussed further in Section IV.

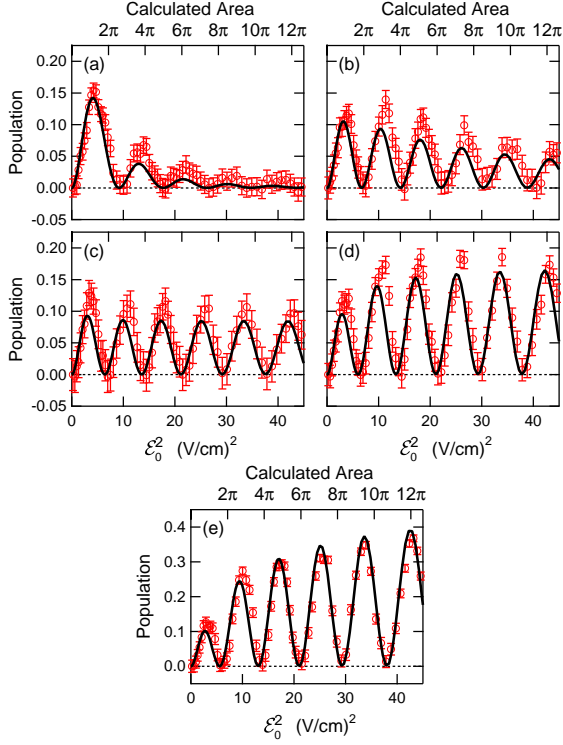


FIG. 6. (Color online) The same as Fig. 3 for 62.5 ns pulses. These pulses have a scaled detuning $\Delta_o\tau/2\pi = 0.5$. The vertical scale for Gaussian results is twice what it is for the other four pulse shapes.

IV. DISCUSSION

A. Scaling of the Rabi Oscillation amplitude

As seen in Figs. 4-7, there are obvious differences in the trends in the amplitude of the Rabi oscillations with pulse intensity depending on small differences in the pulse shape. Numerical results based on Eq. 1 and the model described in Appendix B agree with the trends. More importantly, however, the trends in the maxima of the Rabi oscillations can be understood in terms of the pulse-shape dependent behavior of the states dressed by the pulsed field.

As discussed by Berman et al. [20], to understand our results it is helpful to recast Eq. 1 in terms of the instantaneous eigenstates of the field-interaction Hamiltonian. The eigenvalues of the field-interaction Hamiltonian are $\pm\tilde{\Omega}/2$, where

$$\begin{aligned}\tilde{\Omega}(t) &= \sqrt{\Delta^2(t) + \Omega^2(t)} \\ &= \sqrt{(\Delta_o + \Delta_d G(t))^2 + (\Omega_o G(t))^2}\end{aligned}\quad (15)$$

is the instantaneous energy separation between the two eigenstates.

In this semiclassical dressed-state (adiabatic) basis, the eigenstates are

$$\begin{aligned}|-\rangle &= \cos\theta|i\rangle + \sin\theta|f\rangle \\ |+\rangle &= -\sin\theta|i\rangle + \cos\theta|f\rangle\end{aligned}\quad (16)$$

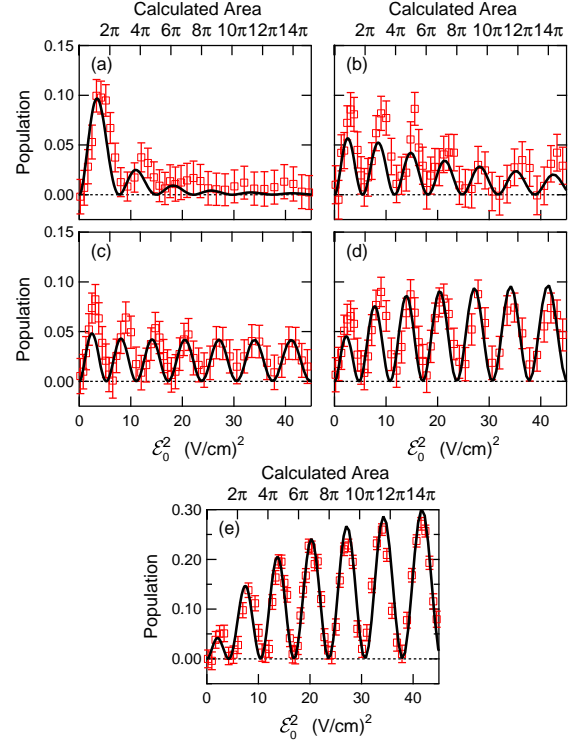


FIG. 7. (Color online) The same as Fig. 3 for 75 ns pulses. These pulses have a scaled detuning $\Delta_o\tau/2\pi = 0.6$. The vertical scale for Gaussian results is twice what it is for the other four pulse shapes.

where the time-dependent mixing angle θ ($0 \leq \theta < \pi/4$) depends on the detuning and the Rabi frequency

$$\tan(2\theta) = \frac{\Omega(t)}{\Delta(t)}. \quad (17)$$

Because the pulses used in the experiments turn smoothly on and off, giving $\theta(\pm\infty) = 0$, the probability amplitudes at the beginning and end of the pulse in the adiabatic basis are the same as the probability amplitudes in the diabatic states.

In the adiabatic basis, the Schrödinger equation is

$$i \begin{pmatrix} \dot{c}_- \\ \dot{c}_+ \end{pmatrix} = \frac{1}{2} \begin{pmatrix} -\tilde{\Omega}(t) & 2i\dot{\theta} \\ -2i\dot{\theta} & \tilde{\Omega}(t) \end{pmatrix} \begin{pmatrix} c_- \\ c_+ \end{pmatrix}. \quad (18)$$

The function $\dot{\theta}$ is a measure of the rate of change of the eigenstates between the zero-field states and the fully-coupled high-field states. Calculated in terms of the parameters of the atomic model and the pulse shape

$$\begin{aligned}\dot{\theta} &= \frac{1}{2} \frac{\Delta\dot{\Omega} - \dot{\Delta}\Omega}{\tilde{\Omega}^2} \\ &= \frac{1}{2} \frac{\Delta_o\Omega_o}{\tilde{\Omega}^2} \dot{G}(t).\end{aligned}\quad (19)$$

We characterize the size of the transition probability be-

tween $|-\rangle$ and $|+\rangle$ with the nonadiabatic coupling function

$$\eta(t) = \frac{2|\dot{\theta}|}{\tilde{\Omega}} = \frac{\Delta\dot{\Omega} - \dot{\Delta}\Omega}{(\Delta^2 + \Omega^2)^{3/2}}. \quad (20)$$

As long as $|\dot{\theta}| \ll \tilde{\Omega}$ ($\eta(t) \ll 1$) at all times during the pulse, then the evolution is adiabatic and $P_- = |c_-|^2$ and $P_+ = |c_+|^2$ remain constant during the evolution, and there are no transitions between states $|i\rangle$ and $|f\rangle$.

Transitions between the two adiabatic states occur when the magnitude of the nonadiabatic coupling is nonzero, which occurs for combinations of a large rate of change of the eigenstates and small differences in the energy. For bell-shaped pulses the nonadiabatic coupling is a double-peaked function of time, with peaks symmetric about $t = 0$ occurring as the pulse turns on and off. Interference between transitions on the rising and the falling edges of the pulse lead to Rabi oscillations. An important observation related to the shape of the nonadiabatic coupling function is that the magnitude of the Rabi oscillations is dominated by behavior in the wings of the pulse when $\dot{\theta}$ is large and $\tilde{\Omega}$ is small, and not where the pulse is most intense, when $\dot{\theta}$ is small and $\tilde{\Omega}$ is large.

We re-express the nonadiabatic coupling in terms of a set of dimensionless parameters

$$\eta(t) = \frac{1}{2} \frac{r}{(\Delta_o\tau)} \frac{|G'|}{[(1 + \sigma r G)^2 + r^2 G^2]^{3/2}} \quad (21)$$

where $\Delta_o\tau$ is the scaled detuning, $r = \Omega_o/\Delta_o$ and $\sigma = \Delta_d/\Omega_o$ are the ratios of the Rabi frequency to the zero field detuning and the peak AC Stark shift to the peak Rabi frequency, and G' is the derivative of G with respect to $x = t/\tau$. For the idealized two-level system $\sigma = 0$, but in our experimental system, $\sigma \approx 0.19$. As might be expected, the nonadiabatic coupling decreases linearly with the scaled detuning independent of the pulse shape. The main question, therefore is how the nonadiabatic coupling depends on the intensity of the pulses.

As a measure of the transition strength, we consider the maximum value of the nonadiabatic coupling function, $\eta(t_o)$, where t_o is the time where the nonadiabatic coupling peaks. In the weak pulse limit, when $r \ll 1$,

$$\eta(t_o) = \frac{1}{2} \frac{S}{(\Delta_o\tau)^2} |G'(t_o)|. \quad (22)$$

In this regime the maximum coupling occurs when G' is a maximum, and for all shapes except the Lorentzian $G'(t_o) \approx 1.5$, and for the Lorentzian, $G'(t_o) \approx 2$. In all cases, the nonadiabatic coupling, and therefore the transition probability, increases with the pulse area as would be expected from the perturbative result of Eq. 4, and decreases with the square of the scaled detuning. For the experimental data presented in Section III, this approximation is valid for $\mathcal{E}_o^2 \ll 4$ (V/cm)².

For strong pulses, when $r \gg 1$, the nonadiabatic coupling peaks further out into the wings of the pulse. The maximum of $\eta(t)$ occurs where $rG(t_o) \approx C$ [20, 42]. The constant

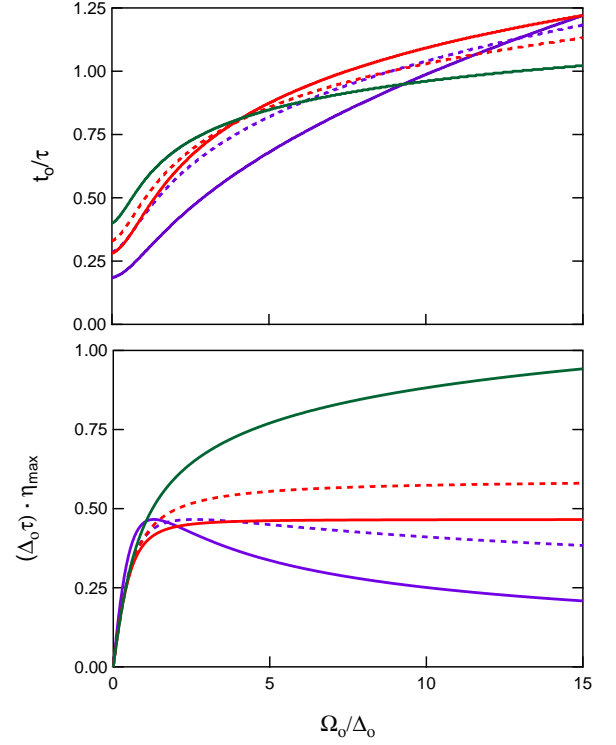


FIG. 8. (Color online) (a) The time of the peak of the nonadiabatic coupling and (b) the size of the peak nonadiabatic coupling multiplied by the scaled detuning *versus* the ratio of the peak Rabi frequency to the zero-field detuning for the five pulse shapes defined in Eq. 13. As in Fig. 2 curves are for Lorentzian (solid, lavender), Lorentzian squared (dashed, lavender), hyperbolic secant (solid, red), hyperbolic secant squared (dashed, red), and Gaussian (solid, green).

$C \approx 1$ is different for each pulse shape and decreases with σ . Fig. 8(a) shows explicitly how t_o/τ increases with r for the five pulse shapes. The results in Fig. 8 are numerical calculations based on Eq. 21, with $\sigma = 0.19$ and are not based on the approximation $rG(t_o) \approx C$.

Using the approximate solution for t_o we find

$$\eta_a(t_o) = \frac{\pi}{\Delta_o\tau} \frac{C_a^{3/2}}{[(1 + \sigma C_a)^2 + C_a^2]^{3/2}} \frac{1}{\sqrt{r}} \quad (23a)$$

$$\eta_b(t_o) = \frac{1}{2\Delta_o\tau} \frac{C_b^{5/4}}{[(1 + \sigma C_b)^2 + C_b^2]^{3/2}} \frac{1}{r^{1/4}} \quad (23b)$$

$$\eta_c(t_o) = \frac{\pi}{2\Delta_o\tau} \frac{C_c}{[(1 + \sigma C_c)^2 + C_c^2]^{3/2}} \quad (23c)$$

$$\eta_d(t_o) = \frac{2}{2\Delta_o\tau} \frac{C_d}{[(1 + \sigma C_d)^2 + C_d^2]^{3/2}} \quad (23d)$$

$$\eta_e(t_o) = \frac{\sqrt{\pi}}{\Delta_o\tau} \frac{C_e}{[(1 + \sigma C_e)^2 + C_e^2]^{3/2}} \sqrt{\ln\left(\frac{r}{C_e}\right)} \quad (23e)$$

for $r \gg 1$. These approximate solutions show, as confirmed by the result of the numerical calculation of $\eta(t_o)$ in Fig. 8(b), that the nonadiabatic coupling behaves differently for the dif-

ferent pulse shapes as a function of pulse intensity. For the Lorentzian and Lorentzian squared pulses, $\eta(t_o)$ decreases with Rabi frequency as $r^{-1/2}$ and $r^{-1/4}$, while for the Gaussian pulse $\eta(t_o)$ increases with the Rabi frequency as $\ln(\sqrt{r})$. Finally, for both the hyperbolic secant and hyperbolic secant squared pulses, $\eta(t_o)$ is independent of r at large intensity.

Physically, the change in the magnitude of the Rabi oscillations is determined by how the rate of change of the eigenstates scales with intensity as the peak of the nonadiabatic coupling pushes farther out into the wings of the pulse. For Lorentzian pulses the rate gets slower as the pulses get more intense. On the other hand, for Gaussian pulses the change becomes more rapid when the coupling is pushed farther out into the wings of the pulse. It is, quite simply, a remarkable property of the structure of the hyperbolic secant pulse that as the peak Rabi frequency increases the nonadiabatic coupling does not change. For other pulses this is simply not the case.

B. Locations of the zeros

The data also shows that, unlike the prediction of the Rosen-Zener conjecture, the return areas are not located at $S_n = 2n\pi$, nor are they evenly spaced in \mathcal{E}_o^2 . This is most apparent in the data for Lorentzian pulses, but can also be measured for the other pulse shapes. In order to demonstrate these variations we plot the first, second, and third return areas for the hyperbolic secant pulse and the Gaussian pulse versus the scaled detuning squared in Fig. 9. In Fig. 10 the first and second return areas for the Lorentzian pulse are plotted versus the scaled detuning. The return areas were calculated using the measured zeros of the peak electric field and the Rabi rate from Eq. 9. Uncertainties in Figs. 9 and 10 are based on the estimated uncertainty in the measured \mathcal{E}_o^2 at the return. These uncertainties characterize the relative difference in the return areas, but there is an additional overall uncertainty of approximately 10% due to uncertainties in the Rabi rate coefficient in Eq. 9 and the field calibration.

Except for the smallest scaled detunings, Gaussian pulses give return areas that are measurably smaller than the return areas for the hyperbolic secant pulses, with the discrepancy increasing with detuning and decreasing with the return number n . For $\Delta_o\tau = 0.6$ the first return for the Gaussian pulse is different by 25% from what is measured for a hyperbolic secant pulse, but only 3.5% different for the third return. As discussed in Section III the first two return areas with the Lorentzian pulse are between 20% and 40% larger than $2n\pi$, and large differences exist even for the smallest experimental detunings.

As described above, Rabi oscillations are due to interference between transitions on the rising and falling edges of the pulse. For the resonant, $\Delta(t) = 0$, case the transition to a 50-50 superposition of the dressed states occurs at $t = -\infty$ and the interference is due to the phase accumulation

$$\Phi_{\text{res}} = \int_{-\infty}^{+\infty} \tilde{\Omega}(t) dt = \int_{-\infty}^{+\infty} \Omega(t) dt = S. \quad (24)$$

For a square pulse with an intensity dependent detuning, the

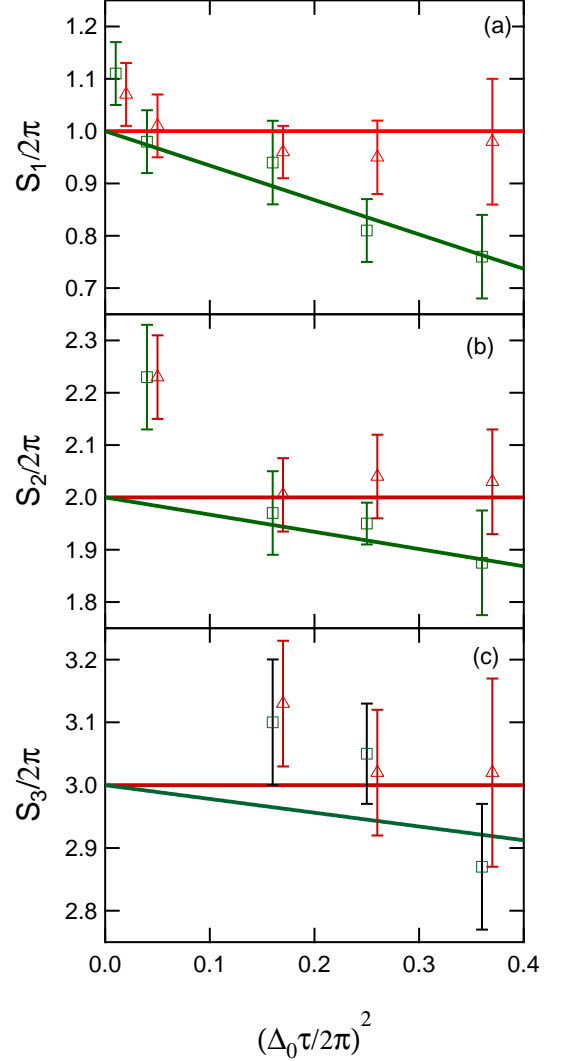


FIG. 9. (Color online) Plots of the return pulse areas (a) S_1 , (b) S_2 , and (c) S_3 for hyperbolic secant (red triangles) and Gaussian (green squares) versus the square of the scaled detuning. A constant line at $S_2/2\pi = 2$ and an approximation for the Gaussian return area based on the calculations of Robinson [24] are shown. For clarity the data points for hyperbolic secant pulses have been offset by 0.01 along the horizontal axis.

coupling projects the states into the coupled basis at $t = -\tau/2$, and the phase,

$$\begin{aligned} \Phi_{\text{square}} &= \int_{-\infty}^{+\infty} \tilde{\Omega}(t) dt \\ &= \int_{-\tau/2}^{+\tau/2} \sqrt{(\Delta_o + \Delta_d)^2 + \Omega_o^2} dt \\ &= \sqrt{(\Delta_o + \Delta_d)^2 + \Omega_o^2} \tau, \end{aligned} \quad (25)$$

accumulates until $t = +\tau/2$ when the states are projected back into the free-atom basis. Returns occur at

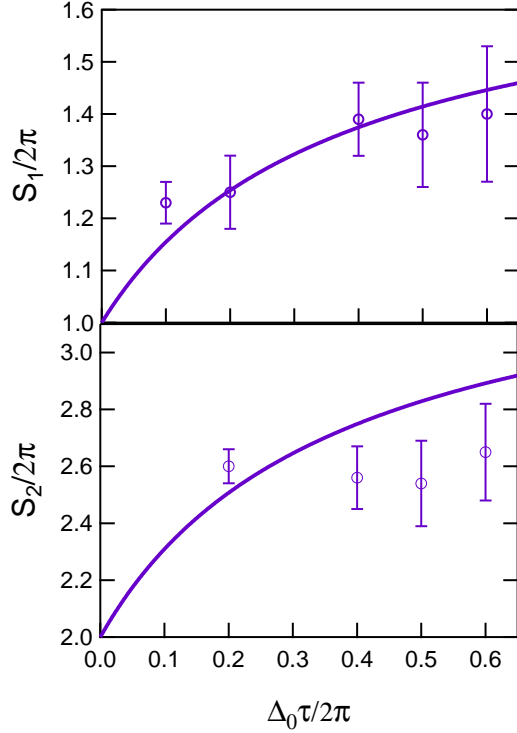


FIG. 10. (Color online) Plots of the return pulse area (a) S_1 and (b) S_2 versus scaled detuning for Lorentzian pulses. Approximations based on the calculations of Robinson [22] are shown.

$\Phi_{\text{square}} = 2n\pi$, corresponding to

$$S_{n,\text{square}} = 2n\pi \sqrt{1 - \frac{1}{n^2} \left(\frac{(\Delta_o + \Delta_d)\tau}{2\pi} \right)^2}. \quad (26)$$

This area is expected from Eq. 7, but clearly different than expected from the Rosen-Zener conjecture.

For other pulse shapes the transition times are not so clearly defined nor are the integrals neatly solved in closed form. However, as discussed above, the nonadiabatic coupling peaks at different times for different detunings, intensities, and pulse shapes, so it is not surprising that the return area would be different for different pulse shapes, even with a constant detuning. It is another remarkable property of the hyperbolic secant coupling with constant detuning that the return areas are not a function of the detuning, but constructive and destructive interference occurs with the same pulse areas as for the resonant case.

A quantitative prediction of the variation in the return areas was made by Robinson [15, 21–24], who reformulated the two-level problem with constant detuning as an eigenvalue problem for S_n^2 . In addition to determining that symmetric pulses always have finite values of S_n for which the population transfer vanishes, he developed a variational method for calculating the eigenvalues for specific pulse shapes. In general, Robinson showed that pulses with Fourier transforms

that are differentiable at $\Delta_o\tau = 0$ have [24]

$$\begin{aligned} S_n^2 &= 4n^2\pi^2 + O((\Delta_o\tau)^2) \\ &\approx 4n^2\pi^2 \left(1 - \frac{1}{n^2} \left(a \frac{\Delta_o\tau}{2\pi} \right)^2 \right), \end{aligned} \quad (27)$$

where a is a constant that depends on the details of the pulse shape. The smoothness requirement makes Eq. 27 invalid for the Lorentzian pulse, which has a discontinuous derivative in its Fourier transform at $\Delta_o\tau = 0$. It is valid for all of the other pulse shapes we used and is also valid for square pulses. Using the known solutions we see that the approximation is exact for a hyperbolic secant pulse with $a = 0$ and for a square pulse with $a = 1$. In the analysis of the data from Gaussian pulses we treat a as a fitting parameter.

Included in Fig. 9 are solid lines at $S_n/2\pi = n$ and a line of the form

$$\frac{S_n}{2\pi} = n - \frac{a^2}{2n} \left(\frac{\Delta_o\tau}{2\pi} \right)^2, \quad (28)$$

which should accurately approximate the theory of Robinson for $(\Delta_o\tau/2\pi)^2 \ll 1$. In Fig. 9(a) the line for the Gaussian pulse is fit to all but the first data point, and gives a value of $a_e = 1.15 \pm 0.03$. In Figs. 9(b) and 9(c), the line for the Gaussian pulse is plotted with a slope of $a_e^2/4$ and $a_e^2/6$ respectively.

Agreement with the form and scaling predicted by Robinson's calculations is quite good considering the uncertainties in the matrix elements used in the calculation and the uncertainty in the experimental electric field. The experimental system also has two important differences from the idealized two-level system. First, in the Raman system the AC Stark shifts increase the rate of phase advance during the pulse over systems without the shifts and therefore shrink the return area, as seen analytically for the square pulse in Eq. 26. Second, the return intensities depend to high precision on the exact values of the parameters in the Hamiltonian and, as discussed below, with the strongest pulses the approximations that go into calculating the parameters of Eq. 9 are not valid.

We have performed sets of numerical experiments which isolate the contributions of the two differences between the physical system and the two-state system with constant detuning. First, we numerically isolated the effect of the AC Stark shifts, by looking at the differences between the two-level system of Eq. 1 with the parameters in Eq. 9 and one in which the AC Stark shifts are artificially eliminated by setting $\Delta_d = 0$. Second, we performed calculations with the two-level approximation of Eq. 1 using the parameters of Eq. 9 and the multi-level model described in Appendix B.

Our first set of calculations shows that the increased separation of the dressed states due to the AC Stark shifts does indeed tend to reduce the return areas over systems with no AC Stark shifts, and that the reduction in return area is greater at larger scaled detuning. We found that the AC Stark shifts reduced the return areas for systems driven by hyperbolic secant pulses by between 5% and 10% in going from a scaled

detuning of 0.1 to 0.6. These calculations agree with the observed result that the return areas for the hyperbolic secant pulse decrease with the detuning.

Changes in the phase advance can be estimated by looking at the difference between the integral of $\tilde{\Omega}(t)$ when AC Stark shifts are present and when they are not. This was done explicitly for the square pulse, and the resulting difference between Eq. 8 and Eq. 26 shows how AC Stark shifts reduce the return area. Because Δ_d increases with pulse intensity it might seem that the largest effect of AC Stark shifts on the return areas would be for the smallest scaled detunings (shortest pulses), which require the largest pulse intensities for a given area. However, with the system we use, an equally important term in the phase advance is the cross-term in the instantaneous frequency separation $2\Delta_o\Delta_d G(t)$ which increases with the scaled detuning.

Our second set of calculations was aimed at understanding why results for the smallest detunings are larger than the return areas for other detunings for both the hyperbolic secant and Gaussian pulse experiments. As seen in Fig. 9, the first return areas for $\Delta_o\tau/2\pi = 0.1$ ($\tau = 12.5$ ns) are about 10% greater than for $\Delta_o\tau/2\pi = 0.2$ ($\tau = 25$ ns). This discrepancy repeats itself for S_2 with $\Delta_o\tau/2\pi = 0.2$ and to a lesser extent for S_3 with $\Delta_o\tau/2\pi = 0.4$ ($\tau = 50$ ns). We note that in the first two cases the return areas occur at very close to the maximum experimental pulse intensity, and in the third case at around two-thirds of the maximum pulse intensity.

As seen explicitly in Figs. 3-7, the scaled results of the multi-level model of Appendix B agrees closely with the experimental return areas, even though these results disagree somewhat with the areas calculated based on the two-level model. The disagreement between the two models at high intensity arises due to the inaccuracy of the approximations made in adiabatically eliminating the intermediate states. As discussed in Appendix A adiabatic elimination of the intermediate states requires that the detunings of the intermediate states from single-photon resonance be significantly larger than the single-photon Rabi rates. The nearest (and most strongly coupled) states to the $23d$ doublet are the $23f$ states which are approximately 7.5 GHz away. The single-photon Rabi rates (Eq. A5) between the $23d$ and $23f$ states increase with linearly with \mathcal{E}_0 with a proportionality of approximately 500 MHz/(V/cm). Therefore, for the largest peak fields used in the experiment the single-photon Rabi rates are approximately half the single-photon detuning, and we expect that the numerical values in Eq. 9 which are used to calculate the pulse area are less accurate at these field strengths. The calculated Rabi rates should be more accurate for the returns as the scaled detuning gets larger, since the fields required for a return are smaller for the longer pulses. We find that the two models agree very well for small intensities, but the two-level approximation gives return areas that are smaller than those from the multi-level model with the discrepancy as large as 12% for the highest experimental pulse intensities.

Given the uncertainties and both of these differences between the experimental system and Robinson's model we should not expect that the agreement will be perfect. However, we do observe a measurable difference in the return areas be-

tween the Gaussian and the hyperbolic secant pulses, and that this difference is largest for the farthest detuned pulses but decrease with return number n .

As discussed earlier, Lorentzian pulses give a much more dramatic difference in the return area than Gaussian pulses, and the sign of the difference is reversed, with return areas larger than for the hyperbolic secant pulse. Using his variational approach Robinson found that Lorentzian pulses have return areas with the explicit form [22]

$$S_n^2 = (2n\pi)^2 \frac{1 + 3|\Delta_o|\tau/\pi}{1 + |\Delta_o|\tau/\pi} + O((\Delta_o\tau)^2), \quad (29)$$

which has a term linear in the scaled detuning.

Also plotted in Fig. 10 is a calculation of the area based on Eq. 29, which contains no fitting parameters. The results agree generally with the predicted values, however as in the results of Fig. 9, the short, high intensity pulses have somewhat larger returns than predicted, and the additional phase advance due to the AC Stark shifts somewhat reduces the return area for the farther detuned pulses. We also expect that corrections to Eq. 29 due to second-order terms in the scaled detuning may be important for the larger detunings.

V. SUMMARY AND CONCLUSION

We have presented experimental measurements of the transition probability of a two-level system driven by pulsed non-resonant electromagnetic fields with five different smooth pulse shapes. By performing the experiments using microwave pulses driving transitions in Rydberg atoms we have been able to make measurements as a function of pulse area with high fidelity of the pulse shape.

With these experiments we have demonstrated that the transition probability between the two levels driven by nonresonant pulses is qualitatively different for different pulse shapes. In contrast with the Rosen-Zener conjecture, for strong pulses the transition probability is not a simple property of the spectrum and area of the pulses. Instead, it depends on the details of how the pulses turn on and off.

Our primary observation is that subtle differences in the pulse shape can lead to dramatic differences in the intensity dependence of the Rabi oscillation amplitude. Following the analysis of Berman *et al.* [20] we have shown that the trends in the dependence of the transition probability with pulse area can be understood with respect to the scaling of the nonadiabatic coupling with intensity. This coupling is a strong function of the rate of change of the eigenstates as the pulse turns on and off. Further we have explicitly demonstrated the contention of Berman *et al.* [20] that the explanation in terms of the scaling of the nonadiabatic coupling is not limited to their model system, but is more generally applicable. The remarkable characteristics of the hyperbolic secant coupling with constant detuning is that there is a balance between the rate of change of the eigenstates and the dressed-state energy levels that leaves the transition probability on the rising and falling edges of the pulse independent of the pulse intensity,

a feature that is not shared by any other pulse shape that we have explored.

By looking at the return areas we have shown that the interference in transitions between dressed-states on the rising and falling edges of the pulses, which is responsible for the characteristic Rabi oscillations, gives oscillation periods that also depend on the pulse shape. The fact that the accumulated phase between transitions on the rising and falling edge is independent of the detuning in the Rosen-Zener solution is also a remarkable property of the hyperbolic secant pulse. We have shown that Gaussian pulses have return areas S_n that decrease subtly with detuning, and that the fractional difference from $S_n = 2n\pi$ is a decreasing function of n . This variation might be expected from the Rabi solution for a square pulse, since the Gaussian pulse has sharper rise and fall, more like a square pulse, than the hyperbolic secant. We have also shown that Lorentzian pulses have return areas that have a remarkably large fractional difference from $S_n = 2n\pi$, and that the fractional difference does not depend on n . Observations for both the Gaussian and Lorentzian pulses are in general agreement with the theory of Robinson, despite the addition of dynamic Stark shifts.

Finally, we have shown that for some pulse shapes, explicitly in the case of Gaussian pulses, that intensity can indeed compensate for detuning and drive transition probabilities that exceed the value for weaker pulses. As shown, the maximum transition probability for Gaussian pulses increases toward unity with pulse area independent of the detuning. Transitions driven by strong Gaussian pulses therefore do not obey the energy-time uncertainty principle which states that the transition probability should exponentially decrease with the scaled detuning.

ACKNOWLEDGMENTS

Special thanks to Paul Berman for many useful discussions. We gratefully acknowledge Wes Campbell, Susan Clark, and Robert Jones for carefully reading and commenting on the text. These experiments were performed with support from the NSF grants PHY-0010007 and PHY-0355160 and from Colby College. Colby College students Melissa Yosua, Roy Wilson, Mao Zheng, and Nick Beard all contributed to the experiment and data acquisition.

Appendix A: The two-level model

In this appendix we develop the equations that lead to the model two-level system described by Eq. 1, which is the basis of a qualitative explanation of the effect of pulse shape on the transition probability.

1. Formalism

In the experiment, a pulsed electric field defined by Eq. 11 drives transitions between an initial state $|i\rangle$ and a final state

$|f\rangle$, separated by energy $E_f - E_i = \hbar\omega_{fi} = \hbar\Delta_o$ via a two-photon process. A single-photon transition between $|i\rangle$ and $|f\rangle$ is not dipole-allowed, but both states are coupled to a group of intermediate states $|k\rangle$ ($k = 1, \dots, N$). We consider the case when all of the intermediate states are far detuned from single-photon resonance. Although the experiments described in this paper are Raman processes, as diagrammed in Fig. 11, the formalism works equally well for two-photon absorption and two-photon stimulated emission.

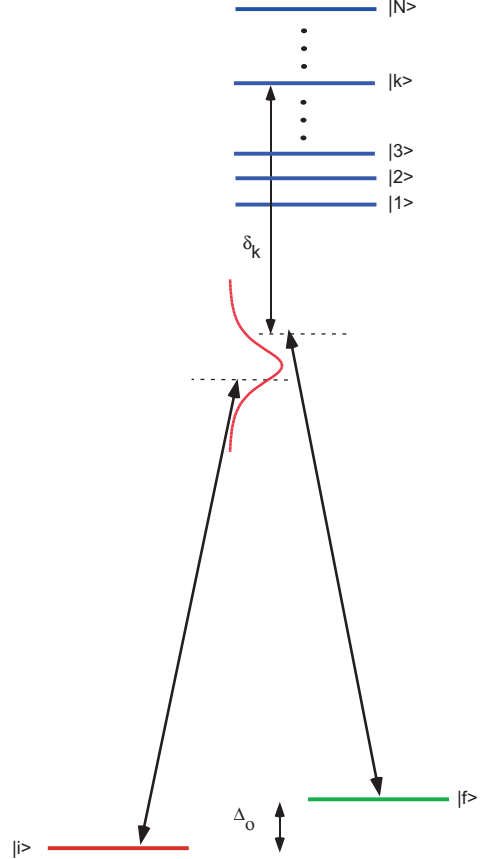


FIG. 11. (Color online) Schematic of the non-resonant Raman transitions driven by the tailored pulses of the experiments. The single photon detuning from an intermediate resonance, $\delta_k = \omega_{kf} - \omega_o$, is very large, while the two-photon detuning Δ_o can be made larger or smaller than the bandwidth of the exciting microwave pulse. In the actual experimental system $\Delta_o < 0$ and some of the intermediate states have energies smaller than states $|i\rangle$ and $|f\rangle$.

The state vector describing the system can be expanded in the interaction representation as

$$\begin{aligned} |\Psi\rangle &= a_i e^{-i\omega_i t} |i\rangle + a_f e^{-i\omega_f t} |f\rangle + \sum_k a_k e^{-i\omega_k t} |k\rangle \\ &= \sum_q a_q e^{-i\omega_q t} |q\rangle, \end{aligned} \quad (\text{A1})$$

where the coefficients a_q are the time-dependent amplitudes of the eigenstates $|q\rangle$ of the atomic Hamiltonian H_{atom} with eigenvalues $\hbar\omega_q$.

The Hamiltonian including the externally applied microwave pulse is given by

$$H = H_{\text{atom}} - \vec{d} \cdot \vec{\mathcal{E}}(t) \quad (\text{A2})$$

in the dipole approximation and the length gauge, where \vec{d} is the dipole operator and $\vec{\mathcal{E}}(t) = \mathcal{E}(t)\hat{e}$ is the electric field defined in Eq. 11. Inserting the state vector of Eq. A1 into Schrödinger's equation gives a set of coupled differential equations for the coefficients a_p ,

$$i\hbar\dot{a}_p = - \sum_q a_q e^{i\omega_{pq}t} \langle p | \vec{d} \cdot \hat{e} | q \rangle \mathcal{E}(t) \quad (\text{A3})$$

where $\omega_{pq} = \omega_p - \omega_q$ are the frequency spacings between the states $|p\rangle$ and $|q\rangle$. Below we will abbreviate the electric dipole matrix elements $\langle p | \vec{d} \cdot \hat{e} | q \rangle$ as d_{pq} .

Because there is no dipole coupling between the initial and final states or between the intermediate states differential equations for the state amplitudes a_p are more specifically written

$$i\hbar\dot{a}_i = -\mathcal{E}(t) \sum_k a_k d_{ik} e^{i\omega_{ik}t} \quad (\text{A4a})$$

$$i\hbar\dot{a}_f = -\mathcal{E}(t) \sum_k a_k d_{fk} e^{i\omega_{fk}t} \quad (\text{A4b})$$

$$i\hbar\dot{a}_k = -\mathcal{E}(t) [a_i d_{ki} e^{i\omega_{ki}t} + a_f d_{kf} e^{i\omega_{kf}t}], \quad (\text{A4c})$$

It is convenient to rewrite the couplings in Eq. A4 in terms of the Rabi frequencies

$$\Omega_{pq} = -d_{pq} \frac{\mathcal{E}_o}{\hbar}, \quad (\text{A5})$$

where \mathcal{E}_o is the peak electric field in the coupling pulse defined in Eq. 11.

The differential equations in Eq. A4 can be numerically solved. However, the computational cost is significant because of the large frequencies ω_{ik} and ω_{fk} relative to the timescale of the dynamics of a_i and a_f . Further, the simplicity of the description as a nearly ideal two-level system is lost.

2. Adiabatic elimination of all intermediate states

In cases where the intermediate states $|k\rangle$ are far detuned from single-photon resonance, they can be eliminated from Eq. A4 and the system approximated as a two-level system. To accomplish the adiabatic elimination Eq. A4(c) is formally integrated by parts, keeping only the boundary term [43]. The remaining integral is negligible if all of the single-photon Rabi frequencies Ω_{pq} and the bandwidth of $g(t)$ are much smaller than the single-photon detunings δ_k . In this case the intermediate state amplitudes a_k adiabatically follow the amplitudes in states $|i\rangle$ and $|f\rangle$:

$$a_k = -\frac{\Omega_{ki}}{2} \left[g \frac{e^{i(\omega_{ki}-\omega_o)t}}{\omega_{ki}-\omega_o} + g^* \frac{e^{i(\omega_{ki}+\omega_o)t}}{\omega_{ki}+\omega_o} \right] a_i - \frac{\Omega_{kf}}{2} \left[g \frac{e^{i(\omega_{kf}-\omega_o)t}}{\omega_{kf}-\omega_o} + g^* \frac{e^{i(\omega_{kf}+\omega_o)t}}{\omega_{kf}+\omega_o} \right] a_f. \quad (\text{A6})$$

Note that to this point, we have retained both the rotating and counter-rotating terms since ω_o is much smaller than ω_{kf} or ω_{ki} . Not making the rotating wave approximation at this stage makes the theory appropriate even when the single photon Rabi rates Ω_{ki} and Ω_{kf} are greater than the photon frequency ω_o [44].

If all of the intermediate states, $|k\rangle$, can be adiabatically eliminated, then inserting the results of Eq. A6 into Eq. A4(a) and A4(b) gives

$$i\dot{a}_i = - \sum_k \frac{\Omega_{ik}\Omega_{ki}}{4} \left[\frac{g^2 e^{-2i\omega_o t}}{\omega_{ki}-\omega_o} + \frac{gg^*}{\omega_{ki}+\omega_o} + \frac{g^*g}{\omega_{ki}-\omega_o} + \frac{g^{*2} e^{2i\omega_o t}}{\omega_{ki}+\omega_o} \right] a_i - \sum_k \frac{\Omega_{ik}\Omega_{kf}}{4} \left[\frac{g^2 e^{-i(2\omega_o+\Delta_o)t}}{\omega_{kf}-\omega_o} + \frac{gg^* e^{-i\Delta_o t}}{\omega_{ki}+\omega_o} + \frac{g^*g e^{-i\Delta_o t}}{\omega_{ki}-\omega_o} + \frac{g^{*2} e^{i(2\omega_o-\Delta_o)t}}{\omega_{kf}+\omega_o} \right] a_f. \quad (\text{A7})$$

A similar differential equation can be derived for a_f .

3. Raman Processes

In a Raman process $\omega_{fi} = \Delta_o \ll \omega_o$. We apply the rotating wave approximation to Eq. A7 by dropping all terms oscillating with frequency $2\omega_o \pm \Delta_o$, and retaining only constant terms and those oscillating at frequency Δ_o . This results in an effective two-level system written in the interaction rep-

resentation as:

$$i \begin{pmatrix} \dot{a}_i \\ \dot{a}_f \end{pmatrix} = \frac{1}{2} \begin{pmatrix} 2\Delta_i G(t) & -\Omega_o^* e^{-i\Delta_o t} G(t) \\ -\Omega_o G(t) e^{+i\Delta_o t} & 2\Delta_f G(t) \end{pmatrix} \begin{pmatrix} a_i \\ a_f \end{pmatrix} \quad (\text{A8})$$

where $G(t) = |g(t)|^2$ is the intensity profile, Δ_p is the peak AC Stark shift of state p

$$\Delta_p = -\frac{1}{2} \sum_k \Omega_{pk} \Omega_{kp} \frac{\omega_{kp}}{\omega_{kp}^2 - \omega_o^2}, \quad (\text{A9})$$

and the peak two-photon Rabi frequency

$$\Omega_o = \sum_k \Omega_{fk} \Omega_{ki} \frac{\omega_{ki}}{\omega_{ki}^2 - \omega_o^2} \approx \sum_k \Omega_{ik} \Omega_{kf} \frac{\omega_{kf}}{\omega_{kf}^2 - \omega_o^2} \quad (\text{A10})$$

The fractional difference between the two expressions for the Rabi frequency in Eq. A10 is of order Δ_o/ω_{kf} which is small in limit of large intermediate state detuning that is necessary for the adiabatic elimination of intermediate states $|k\rangle$.

A final transformation to the field interaction representation is achieved by rewriting the two probability amplitudes

$$a_i = e^{-i\xi_i(t)} b_i \quad (\text{A11a})$$

$$a_f = e^{-i\xi_f(t)} b_f. \quad (\text{A11b})$$

Choosing the phase factors to be defined by

$$\dot{\xi}_i(t) = \frac{1}{2} [\Delta_o + (\Delta_i + \Delta_f)G(t)] \quad (\text{A12a})$$

$$\dot{\xi}_f(t) = \frac{1}{2} [-\Delta_o + (\Delta_i + \Delta_f)G(t)] \quad (\text{A12b})$$

incorporates the phase accumulated due to the zero-field energy-level separation and the average AC Stark shift of the levels.

Rewriting Eq. A8 in terms of the b 's gives Schrödinger's equation in the field-interaction representation:

$$i \begin{pmatrix} \dot{b}_i \\ \dot{b}_f \end{pmatrix} = \frac{1}{2} \begin{pmatrix} -(\Delta_o + \Delta_d G(t)) & -\Omega_o^* G(t) \\ -\Omega_o G(t) & (\Delta_o + \Delta_d G(t)) \end{pmatrix} \begin{pmatrix} b_i \\ b_f \end{pmatrix} \quad (\text{A13})$$

where

$$\Delta_d = \Delta_f - \Delta_i \quad (\text{A14})$$

is the peak differential AC Stark shift.

Appendix B: Computational Model

The two-level model derived in Appendix A is quantitatively accurate for pulses where the single photon Rabi rates of Eq. A5 are much less than the detuning from resonance with the intermediate states and as long as the two photon Rabi rates are much smaller than the driving field's frequency. For the experiments described the second criterion is always fulfilled, but the first is not for the largest pulse intensities. When the single-photon Rabi rates, Ω_{pq} , become greater than 10% of the single-photon detunings then ignoring the boundary term

in the derivation of Eq. A6 makes the simple parametrization of Eq. 9 lose accuracy. In the case of the Raman transitions within the $23d$ Rydberg doublet, the simple adiabatic elimination of the $23f$ doublet loses accuracy compared to the solution of Eq. A4 when fields are greater than a few V/cm.

A second, less important, correction to the two-level system is that some intermediate states are strongly coupled to additional states by the pulse, which changes their energies and distributes their character over several eigenstates. The nl states with $\ell > 3$ are all strongly mixed with the nf state at fields larger than

$$\mathcal{E} = \frac{2}{3} \frac{|\delta_3|}{n^5} \approx 1 \text{ V/cm}, \quad (\text{B1})$$

where $\delta_3 \approx 0.0015$ is the quantum defect of the f state. At these fields the states compose a Stark manifold spread over a frequency band of width

$$\omega_{\text{Stark}} = 3n^2 \mathcal{E} \approx 1.5 \text{ GHz/(V/cm)}. \quad (\text{B2})$$

These shifts and distribution of states are important for the $23f$ states, which are 7.5 GHz away from the $23d$ states, but not for the farther-away f states, which are more than 500 GHz away. The mixing and shifts of these more distant levels do not affect the approximation of Eq. A6 at the level of accuracy of the calculated matrix elements. The intermediate p states have quantum defects a hundred times larger than the f states and therefore negligible shifts or mixing with other states for the field strengths involved.

Figures 3-7 include computed transitions probabilities using a more accurate, but intuitively less helpful model that takes these two corrections into account. This model adiabatically eliminates all the intermediate states but the $23f$ doublet from Eq. A3 and further includes $\ell > 3$ states in the Stark manifold near the $23f$ states. Including these corrections to the Hamiltonian leads to a hybrid set of equations for the system. In this model we integrate the dynamics of the $23d$, $23f$, and 23ℓ states explicitly using Eq. A3, but the additional p and f states are adiabatically eliminated using Eq. A6. The adiabatically eliminated states add an intensity-dependent coupling and relative AC Stark shift parameterized by Ω'_o and Δ'_d to the $23d$ states. Ω'_o and Δ'_d are defined by Eq. A10 and Eq. A9 but excluding the $23f$ states from the summation.

Calculations using this more complex model were used in Figs. 3-7. The calculations based on this model agree with the calculations using the two-level model of Appendix A for low fields, but at $\mathcal{E}_o^2 \approx 40 \text{ (V/cm)}^2$, the zeros of the Rabi oscillations are shifted by more than 10%. On the other hand, the two models give transition probability maxima that are different by less than 3% at all fields.

[1] M. Sargent, M. O. Scully, and W. E. Lamb, *Laser Physics* (Addison-Wesley, Reading, Massachusetts, 1974).

[2] L. Allen and J. H. Eberly, *Optical Resonance and Two-Level Atoms* (Wiley, New York, 1975).

[3] B. W. Shore, *The Theory of Coherent Atomic Excitation* (Wiley, New York, 1990).

[4] N. Rosen and C. Zener, *Phys. Rev.* **40**, 502 (1932).

[5] M. Steffen, J. M. Martinis, and I. L. Chuang, *Phys. Rev. B* **68**,

- 224518 (2003).
- [6] E. Lucero, M. Hofheinz, M. Ansmann, R. C. Bialczak, N. Katz, M. Neeley, A. D. O'Connell, H. Wang, A. N. Cleland, and J. M. Martinis, *Phys. Rev. Lett.* **100**, 247001 (2008).
- [7] K.-M. C. Fu, S. M. Clark, C. Santori, C. R. Stanley, M. C. Holland, and Y. Yamamoto, *Nat Phys* **4**, 780 (2008).
- [8] D. Press, T. D. Ladd, B. Zhang, and Y. Yamamoto, *Nature* **457**, 218 (2008).
- [9] G. D. Fuchs, V. V. Dobrovitski, D. M. Toyli, F. J. Heremans, and D. D. Awschalom, *Science* **326**, 1520 (2009).
- [10] W. C. Campbell, J. Mizrahi, Q. Quraishi, C. Senko, D. Hayes, D. Hucul, D. N. Matsukevich, P. Maunz, and C. Monroe, *Phys. Rev. Lett.* **105**, 090502 (2010).
- [11] R. A. Bartels, T. C. Weinacht, S. R. Leone, H. C. Kapteyn, and M. M. Murnane, *Phys. Rev. Lett.* **88**, 033001 (2002).
- [12] M. Wollenhaupt, A. Prakeit, C. Sarpe-Tudoran, D. Liese, and T. Baumert, *Appl. Phys. B* **82**, 183 (2006).
- [13] C. Trallero-Herrero and T. C. Weinacht, *Phys. Rev. A* **75**, 063401 (2007).
- [14] L. Chuntonov, L. Rybak, A. Gandman, and Z. Amitay, *Phys. Rev. A* **77**, 021403 (2008).
- [15] E. J. Robinson, *Phys. Rev. A* **24**, 2239 (1981).
- [16] A. Bambini and P. R. Berman, *Phys. Rev. A* **23**, 2496 (1981).
- [17] R. T. Robiscoe, *Phys. Rev. A* **27**, 1365 (1983).
- [18] G. F. Thomas, *Phys. Rev. A* **27**, 2744 (1983).
- [19] E. Bava, A. Godone, C. Novero, and H. O. DiRocco, *Phys. Rev. A* **45**, 1967 (1992).
- [20] P. R. Berman, L. Yan, K.-H. Chiam, and R. Sung, *Phys. Rev. A* **57**, 79 (1998).
- [21] E. J. Robinson, *Phys. Rev. A* **29**, 1665 (1984).
- [22] E. J. Robinson, *Journal of Physics B: Atomic and Molecular Physics* **18**, 3687 (1985).
- [23] E. J. Robinson, *Journal of Physics B: Atomic and Molecular Physics* **18**, L657 (1985).
- [24] E. J. Robinson, *Journal of Physics: Condensed Matter* **5**, 13 (1993).
- [25] H. M. Gibbs, *Phys. Rev. A* **8**, 446 (1973).
- [26] Y. S. Bai, A. G. Yodh, and T. W. Mossberg, *Phys. Rev. Lett.* **55**, 1277 (1985).
- [27] T. R. Gentile, B. J. Hughey, D. Kleppner, and T. W. Ducas, *Phys. Rev. A* **40**, 5103 (1989).
- [28] T. H. Stievater, X. Li, D. G. Steel, D. Gammon, D. S. Katzer, D. Park, C. Piermarocchi, and L. J. Sham, *Phys. Rev. Lett.* **87**, 133603 (2001).
- [29] H. Htoon, T. Takagahara, D. Kulik, O. Baklenov, A. L. Holmes, and C. K. Shih, *Phys. Rev. Lett.* **88**, 087401 (2002).
- [30] B. Darquie, M. P. A. Jones, J. Dingjan, J. Beugnon, S. Bergamini, Y. Sortais, G. Messin, A. Browaeys, and P. Grangier, *Science* **309**, 454 (2005).
- [31] I. Gerhardt, G. Wrigge, G. Zumofen, J. Hwang, A. Renn, and V. Sandoghdar, *Phys. Rev. A* **79**, 011402 (2009).
- [32] C. J. Lorenzen and K. Niemax, *Phys. Scr.* **27**, 300 (1983).
- [33] C. W. S. Conover and M. C. Doogue, *Phys. Rev. A* **63**, 032504 (2001).
- [34] M. L. Zimmerman, M. G. Littman, M. M. Kash, and D. Kleppner, *Phys. Rev. A* **20**, 2251 (1979).
- [35] A. Khadjavi, A. Lurio, and W. Happer, *Phys. Rev.* **167**, 128 (1968).
- [36] R. W. Schmieder, A. Lurio, and W. Happer, *Phys. Rev. A* **3**, 1209 (1971).
- [37] N. L. Manakov and V. D. Ovsiannikov, *J. Phys. B* **10**, 569 (1977).
- [38] V. A. Davydkin and V. D. Ovsiannikov, *J. Phys. B* **17**, L207 (1984).
- [39] T. F. Gallagher, L. M. Humphrey, W. E. Cooke, R. M. Hill, and S. A. Edelstein, *Phys. Rev. A* **16**, 1098 (1977).
- [40] C. W. S. Conover, M. C. Doogue, and F. J. Struwe, *Phys. Rev. A* **65**, 033414 (2002).
- [41] C. W. S. Conover and J. H. Rentz, *Phys. Rev. A* **55**, 3787 (1997).
- [42] G. S. Vasilev and N. V. Vitanov, *Phys. Rev. A* **70**, 053407 (2004).
- [43] L. Allen and C. R. Stroud, *Phys. Rep.* **91**, 1 (1982).
- [44] S. Chelkowski and A. D. Bandrauk, *J. Raman Spectrosc.* **28**, 459 (1997).